Measurement of Flow in Microfluidic Networks with Micrometer-Sized Flow Restrictors

Jian-Bin Bao and D. Jed Harrison
Dept. of Chemistry, University of Alberta, Edmonton, Alberta T6G 2G2, Canada

DOI 10.1002/aic.10612

The fluid dynamics in micrometer-sized flow restrictors was evaluated, to test the predictions of the Hagen–Poiseuille equation in small microchip devices. A photobleaching, time-of-flight linear flow rate measurement method was developed for the evaluation of flow in slot-shaped channels with at least one dimension in the size range of 1–3 μm. For a linear flow rate range in the narrowest dimension of 0.3 to 16 mm/s (volumetric flow rates of 0.6 to 32 nL/s, maximum Reynolds number of 0.3), observed flow rates agreed with theoretical predictions within experimental error (2–3%). An empirical equation for the geometric form factor of a D-shaped channel was developed, providing a useful working curve for use of the Hagen–Poiseuille equation in microfluidics design. The Hagen–Poiseuille solution can be used to design multiport devices with intersecting flow channel networks, achieving the intended flow rate ratios in channels with differing flow resistance with an accuracy of 1–2%. Despite the differences between achieved etched dimensions and the nominal design values a deviation of only 1–4% in the flow ratios was also achieved. This observation provides a useful guideline for predicting tolerance sensitivity in device manufacture. © 2005 American Institute of Chemical Engineers *AIChE J,* 52: 75–85, 2006

Keywords: microfluidics, nonslip boundary condition, velocimetry, photobleaching velocimetry, flow restrictor design

Introduction

Control of the direction of fluid flow within a network of flow paths in a microfluidic device is paramount to its proper operation.[1] Control of pressure-driven flow requires active valving, or else passive control, through variation of the flow resistance of each intersecting channel by adjusting the channel's geometry. Flow restrictors in a microfluidic system must have at least one dimension of a few micrometers or less, given typical channels sizes of 10–300 μm. To achieve rational design of passive flow control with such flow restrictors, an accurate model describing fluid flow must be available. The Navier–Stokes equations provide the basis for modeling fluid flow, and their common solutions in the form of the Hagen–Poiseuille equations are routinely used to describe flow.[2,3] However, two recent reviews on flow in microfluidic systems indicate there is some controversy as to whether these equations are entirely suitable. Stone et al.[4] conclude that the traditional nonslip boundary conditions apply in all but the most unusual cases, whereas Squires and Quake[5] acknowledge considerable controversy in the literature, and suggest that for smaller dimensions these issues are not yet settled.

Pfahler et al.[6] evaluated flow in microchannels 0.8 and 1.7 μm deep, and 100 μm wide, reporting significant deviations of nearly +300 and −20%, respectively, from predictions based on the Navier–Stokes equations. Several studies in channels with hydraulic diameters of 50–250 μm showed there is a modest deviation in friction factor from Poiseuille flow theory, and that the onset of turbulent flow may occur at much lower Reynolds number than expected.[7-10] Others also observed friction coefficients larger than predicted by the Navier–Stokes equations.[11,12] These deviations have been ascribed to the effects of surface roughness, double-layer effects on surface viscosity, and entry effects. Very recently, Kohl et al.[13] sug-

---

gested most of the inconsistencies are the result of instrumentation errors, in that their own observations showed no significant deviations for microchannels with a hydraulic radius of 25–100 μm. Choi et al.[14] also concluded that nonslip boundary conditions and the Hagen–Poiseuille equations described 1 μm deep channels when the channels were hydrophilic, but not when the channels were hydrophobic. These uncertainties require an evaluation of the suitability of the Poiseuille solutions to the Navier–Stokes equations for use as a design tool for microchannels with dimensions on the scale of 1 μm. Systematic errors in the measurements methods used with very small volumes certainly may play a role in the current controversy, and so our efforts have in part focused on developing a measurement technique that is well adapted to microfluidic scales.

Evaluation of the Navier–Stokes equation and its solutions requires accurate measurement of the relationship between flow rate and pressure. A variety of particle-based techniques, such as particle imaging velocimetry (PIV)[15,16] or laser Doppler[17,18] methods, have been applied in chips with dimensions > 10 μm. However, particles should be much smaller than 1 μm to evaluate a 1-μm flow path, making such methods less suitable. Here we have used a time-of-flight approach, in which photobleaching creates a dye zone of reduced concentration in a flowing fluorescent dye stream, whose time of travel can be monitored with fluorescence detection. The method is related to that of optical gating used by Monnig and Jorgenson,[19-21] and to transport studies using optically released caged fluorescent dye, but instead uses fluorescein photobleaching.

Because 1 μm deep channels are very susceptible to plugging, devices were designed with a short, shallow weir zone (1–3 μm deep, about 280– 290 μm wide, and 18–32 μm long) to create the flow constriction, accessed with 10 μm deep channels in which the flow measurements were made. Flow in such broad shallow channels can be approximated as two-dimensional flow, and will be termed *slot flow* here. Linear flow rates measured in these straight channels were quantitatively compared to the predictions of the Hagen–Poiseuille equation for rectangular geometries using the equations developed below. Flow rates were then measured within a network of channels and flow restrictors, and the resulting values were compared to predictions based on the Hagen–Poiseuille equation. A three-port, double-weir device we have developed for liquid chromatography, electrochromatography, and other applications[22,23] was used for those tests. Wide channels in that device could be described as rectangular, but channels with an aspect ratio (width to depth) >0.1–0.2, prepared by isotropic etching,[24] have a D-shape that is not treated by published solutions to the Navier–Stokes equation. To account for the effect of this shape, computational fluid dynamics modeling[3,25] was used to provide a working curve relating the geometric form factor for a D-shaped channel to that of a rectangular channel with the same aspect ratio of depth to width (d/W). This report thus presents a means to measure linear flow velocity within a microfluidic chip, correlates linear velocity with volumetric flow rate, evaluates the accuracy of the Hagen–Poiseuille equation in 1 μm deep flow channels, and tests the model's ability to describe the proportioning of flow within a network of flow channels.

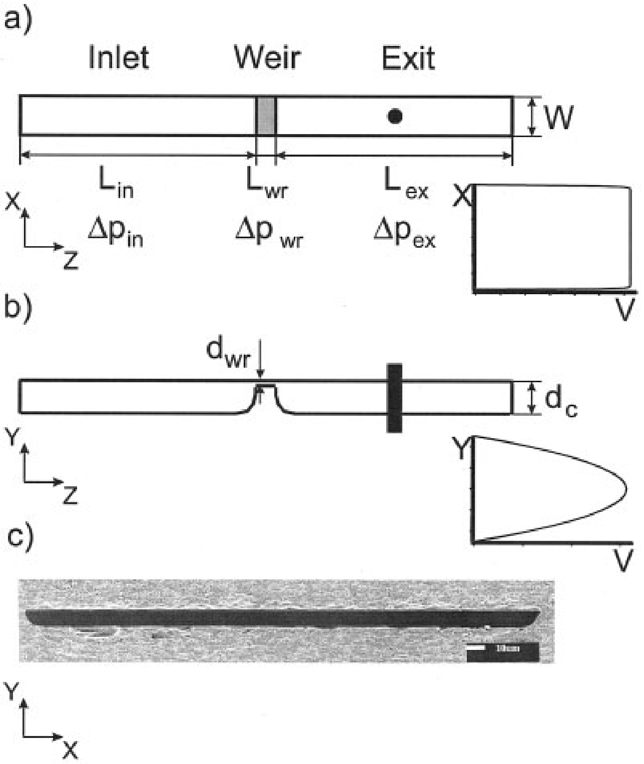

Figure 1. Geometry of single channel layout.

Diagram shows the inlet (in), exit (ex), and weir (wr) segments. Also shown are the coordinate system, pressure drops, and channel dimension symbols used in the mathematical analysis. Nominal channel width and depth were 290 and 10 μm, respectively. Weirs were nominally either 1 or 3 μm deep. The insets show (a) the flow profile along the *x*-direction, top view calculated using Eq. 2; and (b) along the *y*-direction, side view, as calculated from the solution to Eq. 1. The solid circle and bar show the laser spot used to measure flow velocity. The lowest image (c) shows an electron micrograph of the wide channel cross section.

Theory of Flow Velocity Parameters Measured in Slot Flow

The flow velocity measurement method employed in this study evaluated the flow rate in the center of a wide, shallow, rectangular channel, which exhibits slot flow. To evaluate the measured linear velocity of a moving dye front, the solutions to the Navier–Stokes equation were evaluated to obtain the average flow across the channel depth (y-direction), and the maximum velocity across the channel width (x-direction). The coordinate system is defined in Figure 1. For an incompressible, constant-viscosity fluid flow through a rectangular cross section, the Navier–Stokes equation and nonslip boundary condition can be written[2] as

$$\frac{\partial^2 V_z}{\partial x^2} + \frac{\partial^2 V_z}{\partial y^2} = \frac{1}{\eta}\left(-\frac{dp}{dz}\right) \tag{1}$$

with $V_z = 0$ at $x = \pm W/2$ and $y = \pm d/2$, where V_z, p, and η stand for the velocity along the flow channel, the pressure, and the viscosity of the liquid, respectively. W and d are the width and depth of the channel.

Solving Eq. 1 and then integrating across the y-direction yields the velocity as a function of x, averaged across the y-direction ($\overline{V_z}(x)$):

$$\overline{V_z}(x) = \frac{d^2}{4\eta}\left(-\frac{dp}{dz}\right)\left\{\frac{1}{3} - \frac{32}{\pi^4}\sum_{n=0}^{\infty}\frac{\cosh\left[\frac{(2n+1)\pi x}{d}\right]}{(2n+1)^4\cosh\left[\frac{(2n+1)\pi W}{2d}\right]}\right\} \equiv \frac{d^2 G(x)}{4\eta}\left(-\frac{dp}{dz}\right) \quad (2)$$

where the function $G(x)$ is a maximum at the center of the channel ($x = 0$). However, for slot flow, $G(x)$ varies rapidly only at the channel edges, and is close to constant across most of the channel, as illustrated by an inset in Figure 1. Thus, for a measurement made near the center of the channel, as is the case for the fluorescence probe technique used in this study, the linear flow velocity observed is given by

$$\overline{V_z}(0) = \frac{d^2}{4\eta}\left(-\frac{dp}{dz}\right) \times \left\{\frac{1}{3} - \frac{32}{\pi^4}\sum_{n=0}^{\infty}\frac{1}{(2n+1)^4\cosh\left[\frac{(2n+1)\pi W}{2d}\right]}\right\} \quad (3)$$

Equation 2 may be further integrated over $x = -W/2$ to $+W/2$ to give the Hagen–Poiseuille equation[2,3]

$$Q = \frac{W^2 d^2 F}{4\eta}\left(-\frac{dp}{dz}\right) \quad (4)$$

where Q is the volumetric flow rate and F is a geometric form factor for a rectangular channel given by

$$F = \frac{W}{3d} - \frac{64W^2}{\pi^5 d^2}\sum_{n=0}^{\infty}\frac{\tanh\left[\frac{(2n+1)\pi d}{2W}\right]}{(2n+1)^5} \quad (5)$$

Equations 4 and 5 show that the volumetric flow rate is a complex function of the aspect ratio of the channel (d/W) and the square of the cross-sectional area (Wd). For a channel with a constriction along the flow path, such as the devices studied here, the volumetric flow rate (Q) through each region must still be equal. Referring to Figure 1 we can write

$$\Delta p = \Delta p_{in} + \Delta p_{ex} + \Delta p_{wr} \quad (6)$$

where the subscripts *in*, *ex*, and *wr* refer to pressure drops in the inlet, exit, and weir segments of the channel, respectively. Assuming each channel segment is long enough for flow to become fully developed so that the pressure gradient is linear along the segment, the differential in Eq. 4 becomes $\Delta p_i/L_i$, where i refers to a given channel segment, L_i is its length, and Δp_i is defined as the high p minus the low p. Using Eq. 4 we can also write

$$\Delta p_{in} + \Delta p_{ex} = \frac{4\eta(L_{in} + L_{ex})Q}{W^2 d_{in}^2 F_{in}} \quad (7)$$

given that, in our devices, W and d up- and downstream of the weir were the same. The fraction of pressure drop across the deeper channel segments is given by combining Eqs. 6 and 7 to obtain

$$\frac{\Delta p_{in} + \Delta p_{ex}}{\Delta p} = \frac{(L_{in} + L_{ex})}{d_{in}^2 F_{in}} \Bigg/ \left[\frac{(L_{in} + L_{ex})}{d_{in}^2 F_{in}} + \frac{L_{wr}}{d_{wr}^2 F_{wr}}\right] \quad (8)$$

Equation 8 relates the pressure drop in the deep channel segments to the total pressure drop along a channel. Used in combination with Eq. 3, and recognizing that dp/dz is a constant in the deep channels given their equal cross sections, we obtain a relationship between the observable parameters of linear velocity $\overline{V_z}(0)$ and total pressure drop

$$\overline{V_z}(0) = \frac{\frac{1}{F_{in}}}{\frac{4\eta(L_{in} + L_{ex})}{d_{in}^2 F_{in}} + \frac{4\eta L_{wr}}{d_{wr}^2 F_{wr}}} \times \left\{\frac{1}{3} - \frac{32}{\pi^4}\sum_{n=0}^{\infty}\frac{1}{(2n+1)^4\cosh\left[\frac{(2n+1)\pi W}{2d_{in}}\right]}\right\}\Delta p \quad (9)$$

Evaluation of the quantitative relationship between these two measured variables can then be used to determine the suitability of the Navier–Stokes and Hagen–Poiseuille equations for describing flow in micrometer-scale channels.

Experimental

Device fabrication

Devices were fabricated in Corning 0211 glass (Corning Glass, Parkridge, IL) at the University of Alberta NanoFab Lab, using published procedures.[24] A two-mask process was used to fabricate the weir structure. Channels were etched to approximately 10 μm deep, and weirs were etched to either 1 or 3 μm deep; exact depths were determined using an Alpha Step 200 profilometer (Tencor Instruments, San Jose, CA) to a precision of ±0.01 μm. Channel and weir dimensions were determined by optical microscopy, using a reticle and etched scale, and were confirmed by electron microscopy (JEOL X-version JSM 6301 FXV, Peabody, MA) to precisions of 0.5 μm or 20 nm, respectively. A two-port, single-channel design illustrated in Figure 1 was used, with typical channel widths of 290 μm and weir lengths of 19–32 μm. For three-port devices typical, approximate widths were 600 μm for the inlet and outlet channels, 280 μm for the weirs, and 40 μm for the side channel.

Reagents

Fluorescein disodium salt (Sigma, St. Louis, MO) was used as received. Distilled water was polished with a Milli-Q UV Plus Ultra-Pure Millipore system (Mississauga, Ontario, Can-

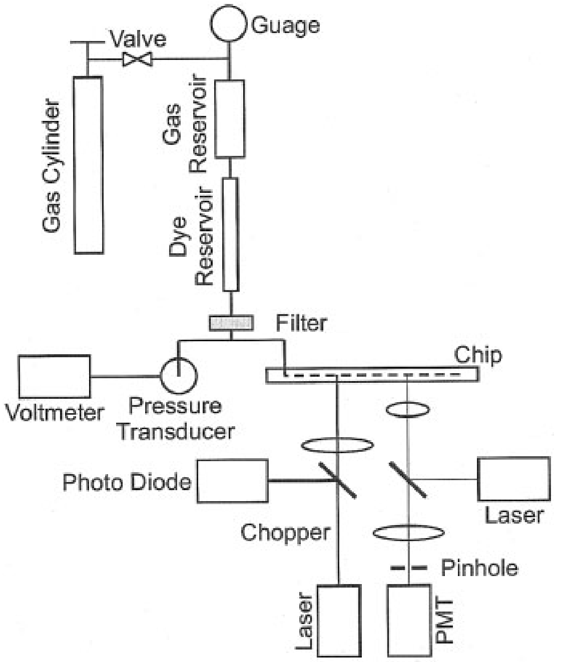

Figure 2. Apparatus used for time-of-flight, photobleaching velocity measurement.

Pressure was developed with a gas cylinder, reservoirs were made from polyethylene tubing, and a 0.5-μm filter was used to remove particulates. Two lasers and a variety of lenses were used for photobleaching and fluorescence detection. A micrometer was used to set the distance between the bleaching and fluorescence detection spots.

ada). The water used as solvent was prepared by mixing fully degassed water and fully oxygen saturated water in a 1:1 ratio, into which fluorescein was dissolved at 190 nM. Polished water was degassed by boiling, transferred to a centrifuge tube and capped with no included air volume, then cooled in a water bath to room temperature. A portion of the degassed water was fully oxygen saturated by sparging with O_2 (Praxair, Mississauga, Ontario, Canada) overnight. Solutions were passed through a 0.22 μm pore size filter (Millipore, Bedford, MA) before being introduced to the dye reservoir.

Pump system and microchip operation

Figure 2 illustrates the constant-pressure pump system used. A gas cylinder and regulator were used to pressurize a gas and solvent reservoir, consisting of a poly(ethylene) tube (7 mm OD, 5 mm ID, $\sim$35 cm length) and a copper tube connected to the regulator, with a total volume of about 13.5 mL. The aluminum foil–wrapped plastic tube was charged with 3 mL of solution, the system sealed, and the regulator opened. Once pressure reached the required value a valve was closed to isolate the gas and liquid reservoirs from the cylinder. At the highest flow rate, pressure dropped by $<$0.3% over the course of measurement, and no pressure change was observed at mid- or low-flow rates. A frit-in-a-ferrule (0.5 μm pore size, Upchurch, Oak Harbor, WA) was added upstream of the pressure sensor. A micropressure transducer (NPC-1210-015-D-3L, Lucas, Fremont, CA) monitored the pressure drop across the device relative to the atmosphere, using a 10 ppm resolution voltmeter (Hewlett–Packard Model 3468A Multimeter, Palo Alto, CA) for readout. The transducer was calibrated with a Hg-filled U-tube connected in place of the chip, mounted vertically using a plumb bob, interpolating to 0.2 mm using graph paper marked to 1-mm resolution for a scale. The transducer was always kept on after each calibration. The chip was mounted in an aluminum holder and a flangeless nut and a frit-in-a-ferule coupling (Upchurch) was used to connect the pressurized source to the inlet. Room temperature was monitored by a thermometer (0.01K, VWR), to allow selection of water-viscosity values from tabulated results.

Linear flow velocity measurements

The time of flight of a photobleached zone of dye was measured to determine velocity. A 190 nM fluorescein solution proved to be optimal: dilute enough to reduce dye–dye interactions that result in aggregate formation[26-28] during photobleaching, but high enough to give a strong signal. A 50% O_2-saturated solution was used to reduce dye aggregate formation because O_2 reaction with the excited optical state competes with dye–dye interactions. Higher O_2 concentrations caused bubble formation at the weirs. Figure 2 illustrates the time-of-flight detection apparatus. Two 488-nm Ar-ion lasers (Uniphase-Cyonics, San Jose, CA) were used; one laser operated at 2.5–12 mW was focused (plano-convex, $f = 150$ mm; Newport, Irvine, CA) to a 50 μm diameter spot to photobleach the dye. The intensity increased as the flow rate was increased. A chopper was operated at 0.5 Hz to generate a square-wave dye concentration variation, alternately directing the beam between the chip and a photodiode (3 mm diameter, Silicon Detector Corp., Newbury Park, CA). The second laser ($\sim$2.5 mW, $\sim$25 μm spot size) was used for laser-induced fluorescence detection using a custom-built inverted, confocal, epiluminescent, infinite optical conjugation microscope.[29] A 10 × objective (5709, New Focus, Santa Clara, CA), 20 cm f.l. tube lens (Achromat PAC064, Newport) and a 200-μm pinhole (Newport) were used to observe a 20-μm detection zone. The distance between the bleaching point and the detection points was set using a calibrated translation stage (423 stage with SM-13 micrometer; Newport), with a positioning error < 1 μm. Signals, shown in Figure 3, were monitored with a Pentium 1, 75-MHz computer, equipped with a National Instruments PC+ board, and Labview Software v.4 (Austin, TX). A 25-kHz acquisition rate was used, but 250 points were averaged in blocks to yield a 100-Hz net acquisition rate. Data were processed using Origin v5.0 (Microcal, Northampton, MA) by differentiation, using a 13-point Savitsky–Golay algorithm included with Origin, to allow ready determination of the edges of the photobleached spot. Data were measured first 1 mm away from the bleaching point, and the time of flight from the bleached spot was determined for about five pulse periods. The detector was then translated 2.000 mm away from the first observation point, and time of flight was again determined from the bleached spot. These measurements were more than 1 cm downstream of the weir for the single-channel devices. For the three-port devices a pair of such measurements were made first 1 cm upstream and then 1 cm downstream of the weir structures, and at least 1 cm from any corners. Because photoproducts could plug the weir, measurements upstream of the weir in the three-port device were limited to durations of 1 min at each pressure. No plugging, as evidenced by stable flow rates

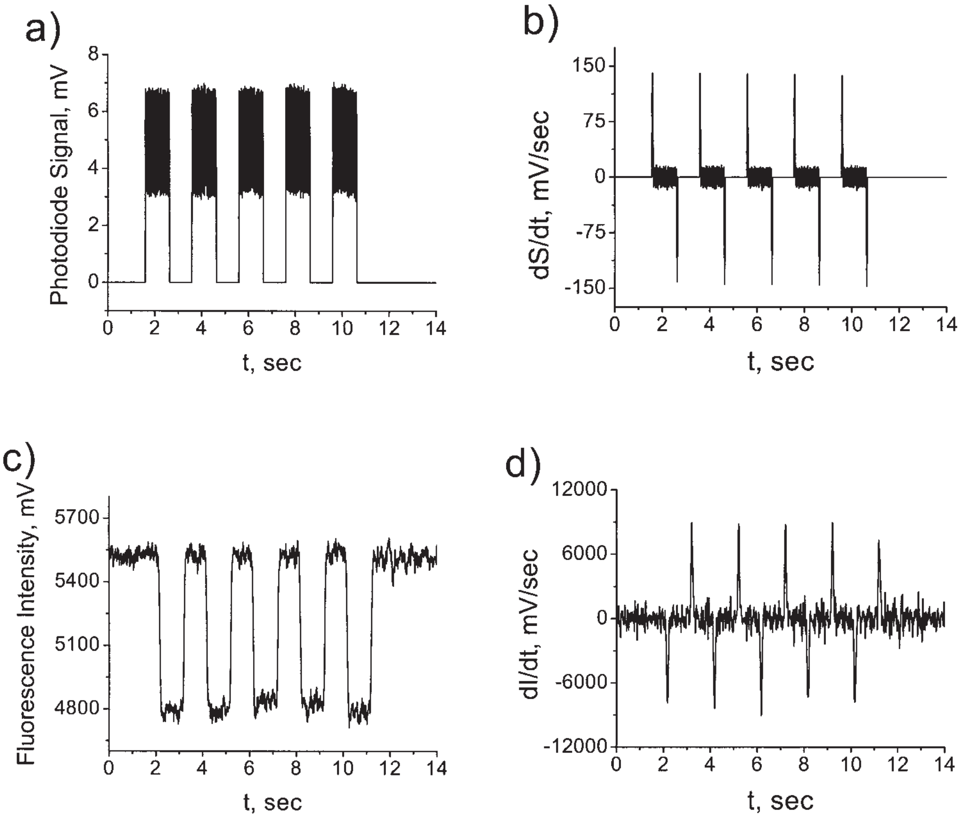

Figure 3. Four images illustrating the time-of-flight measurement of flow velocity.

(a) Chopped laser beam used to bleach dye upstream of the weir, measured with a photodiode; (b) differentiated photodiode signal used to highlight edges of the bleached spot; (c) fluorescence intensity measured downstream of bleaching spot; (d) differentiated fluorescence signal used to highlight edges in the bleached spot rise and fall. The time required for the edge to travel from the bleaching point was used to determine flow velocity, according to the specific method described in the text, Eq. 10.

over time, was seen when measurements were made downstream of the weir.

Finite-element modeling

FlumeCAD software (Version 4.8.3, Coventor, Raleigh, NC) was used for simulating the D-shaped cross section generated by isotropic etching. Linear flow velocity was the only numeric output readily supplied by the software.[30] Consequently, two simulations were made in parallel for each given channel dimension simulated; in one a pressure (typically 1 Pa) was applied, in the other a volumetric flow rate (typically 1 pL/s) was used. The linear flow velocity output in numeric form from both runs was then used to establish the relationship between pressure and volumetric flow rate. The pressure–flow rate relationship obtained was then compared to the Hagen–Poiseuille equation for rectangular flow channels and an effective form factor, F_D, for a D-shaped cross section was determined. Simulations were performed on a Sun Microsystems Ultra 10 (Palo Alto, CA), using a depth of 10 μm, a variable width, and a length ten times the width.

Choosing the proper mesh size is important for a finite-element method (FEM). All channel dimensions were simulated for both rectangular and D-shapes, and the results for the rectangular shape were compared to the results of the Hagen–Poiseuille equation. The mesh was adjusted until the results of the simulation and the Hagen–Poiseuille equation agreed within 3%. The ratio between simulated and calculated results was used to correct the simulated values for both rectangular and D-shaped channels of the same aspect ratio. For example, for a d/W ratio of 0.333, using 36 elements in the cross section gave simulations that matched the Hagen–Poiseuille equation, as long as there were >30 elements along the direction of flow. When the number of elements along the flow was only 10, the calculation was stable only when the number of cross-sectional elements was >60. We thus selected 60 elements in the cross section and 30 elements along the flow direction. A 27-node brick was used as the element and a parabolic function was used for interpolation during the simulation. Larger numbers of nodes, or longer channels, tended to produce out-of-memory errors. This same approach was applied to all channel geometries, and we achieved $<3\%$ deviation for all but one case. For an aspect ratio of 0.05 a 10% deviation between simulated and calculated values was accepted because the mesh could not be set finer as a result of memory constraints.

Results and Discussion

Our evaluation of the use of fluid restrictors to control flow in microfluidic devices, and the appropriateness of using the predictions of the Navier–Stokes equation to design such flow restrictors, can be broken down into several steps. We first needed to develop a method to accurately measure flow velocity within the microchannels. The flow rates measured in a straight line channel with a single constriction were then quantitatively compared to the predictions of the Hagen–Poiseuille equation, to establish the relevance of the equation for flow in the microchip. Finally, flow rates were measured in a network of channels and flow restrictors, and the resulting values were compared to predictions based on the Hagen–Poiseuille equation. Computational fluid dynamics modeling was required to accurately make the latter assessment, given the nonrectangular cross section of small, isotropically etched flow channels. Each of these steps is discussed in detail below.

Flow rate measurements

Linear flow velocity was measured using a fluorescent dye and a photobleaching technique to create a plug of reduced dye concentration. The time of flight of the bleached plug was then determined by measuring at two locations downstream of the bleaching site, allowing the velocity to be determined using the following equation:

$$V = \frac{L_2 - L_1}{t_2 - t_1} \tag{10}$$

The locations L_1 and L_2 were 1 and 3 mm downstream of the bleaching spot, respectively, whereas t refers to the time the edge of the bleached zone transits the detector at that location. Figure 3 illustrates the laser bleaching pulses generated by a chopper, and the fluorescence changes observed downstream as a result of bleaching. To improve precision, the data were differentiated, and the peaks were used to determine the edges of the bleached zone, as indicated in Figure 3d. The phase shift in the position of the edges for any given bleached zone gave the time t_1 or t_2 required to travel from the bleaching zone. Although absolute values relative to the bleaching spot could have been used, Eq. 10 gives greater precision because the distance between the two detection zones can be set within 1–2 μm. Additionally, for greatest accuracy we require that relaxation of the shape of the bleached zone arising from Taylor dispersion be fully developed in the directions perpendicular to the direction of flow. At both detection zones this is the case, as discussed below.

The channels used for velocity measurements in this study are slot shaped, being much wider than they are deep. The slight deviation from a rectangular shape as a result of isotropic etching of the channels, illustrated in Figure 1, can be neglected in slot flow. Across the width of the channel, the x-direction, slot flow gives a nearly uniform flow velocity profile, making the measurement independent of exact position near the channel center, and tolerant of the finite size of the measuring spot. Calculations using Eq. 2 indicate the flow velocity $\overline{V_z}(x)$ is essentially constant across nearly 80% of a 200 μm wide inlet and outlet channels. So for channels 280 μm wide or more we were readily able to use a bleaching laser spot size of 50 μm and a fluorescent measurement (probe) spot size of about 20 μm. In the vertical direction, the y-direction, the fluorescence measurement will give the average velocity as given by Eq. 3.

Flow velocity must be measured in a region of fully developed flow, unaffected by entrance effects and other factors. For a Reynolds number near zero, the flow velocity profile is considered to have reached steady state after a length of 0.6d, where d is the characteristic dimension of the flow channel.[31,32] For an average linear flow rate of 10 mm/s in the inlet channel, with a 20-μm characteristic dimension, using a density ρ of 10^3 kg/m^3 and a viscosity η of 10^{-3} Pa·s, gives Re = 0.2, and an entrance length of 12 μm. For the same Reynolds number within the weir region, a 1 μm deep weir requires a 1.2 μm entrance length, whereas a 3 μm deep weir requires 3.6 μm. Thus, the 19–32 μm long weirs used in this study will reach fully developed flow. Downstream of the weir at Re = 0.2 the entrance length is again 12 μm. The detector was located at least 1 cm from the weir, so that flow velocity was fully developed at the measurement point and in each channel segment.

The concentration plug generated by photobleaching must become fully developed in terms of radial (or lateral) Taylor–Aris dispersion, and so we must consider diffusion in the radial direction to evaluate the required distance downstream. Figure 1 illustrates the coordinate system used in this analysis. Diffusion in the z-direction reduces the magnitude of the fluorescence signal change caused by bleaching, but does not affect the travel time. In the x- and y-directions, the velocity vectors are zero. Given that we have slot flow and are measuring near the center of the channel there is no local concentration gradient in the x-direction. As a result the relevant time-dependent concentration term for establishing a fully developed plug profile, $\partial C/\partial t$, is governed primarily by diffusion in the y-direction and must be of the same order as $D_f(\partial^2 C/\partial y^2)$, where D_f is the dye diffusion coefficient.[33] Near the top and bottom edges of the flow channel, where $y \sim \pm d/2$ we have, by analogy to the case for a cylindrical geometry

$$\frac{L_D}{V_z} \sim \frac{(d/2)^2}{D_f} \tag{11}$$

where L_D is the required distance downstream from the bleaching zone for fully developed flow. For the channel depth of 10 μm used here, a typical higher velocity of 10 mm/s, and a fluorescein diffusion coefficient of 3.3×10^{-10} m^2/s,[24] the development length is about 760 μm. So the initial detection point 1 mm from the bleaching point should be sufficiently far downstream. In fact, no deviation was observed even at a velocity of nearly 15 mm/s, as seen in Figure 4.

Figure 4 shows typical velocity–pressure responses for a 3 μm deep weir device; complete dimensions are given in Table 1. Each data point is the average of about 30 individual velocity measurements and has a precision of ±0.5%. Individual curves show extremely high linearity, with r^2 = 0.9999 to 1.0000, and a typical relative standard deviation (RSD) in the slope of ±0.5%. The intercepts were always within 1 SD of zero. There was some change in slope over time, with an RSD of ±2.6% measured over a 5-day period. This variation appeared to arise from contamination of the channels and weir attributed to flow of solvent, requiring careful preparation of the solutions to achieve a variation this small. These data indicate our apparatus can provide reproducible measurements of the linear velocity in a slot-shaped microchannel.

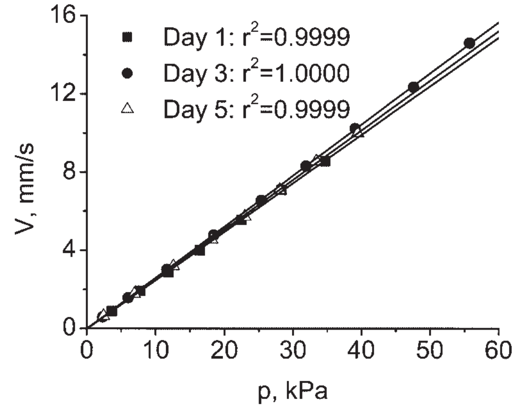

Figure 4. Plot of flow velocity vs. applied pressure.

Data are for a two-port, single-channel device (Figure 1), determined on three different days (T = 23.5, 24.3, and 23.0°C), illustrating the very small deviations observed over time. Device 9A: 3 μm weir depth; see Table 1 for other dimensions. Bleaching laser 10 mW, detection laser 2.5 mW, PMT bias 500 V. Variation in slopes was ±2.6%.

Comparison of experimental flow velocity with the Hagen–Poiseuille equation

The flow velocity was determined as a function of pressure for four different device layouts with the layout shown in Figure 1, and specific dimensions given in Table 1. The weir acted as a flow restrictor, reducing the slope of the velocity–pressure curves as the weir depth decreased or the weir length increased. The observed slopes are reported in Table 2. The volume flow rate and pressure relationship that is predicted according to the Hagen–Poiseuille equation can be related to the linear flow rate vs. pressure using Eq. 9, developed earlier in the Theory section. Because of the low fluorescein concentration the viscosity used was that of pure water. The measured device dimensions were used in the calculation, assuming a rectangular shape. The calculated slopes are also reported in Table 2, along with the percentage deviation of the calculated value relative to the experimental value.

The deviation between theory and experiment indicated in Table 2 is ≤3%. Experimental error for any given slope is <0.5%, but the variation of slope over time of ±2.6% is a more reliable estimate of the absolute precision of each measurement. Thus, the observed deviations are within our estimated experimental error. Although some local heating as a result of photobleaching is expected, the magnitude of temperature change should be in the range of 0.1 to 0.3°,[35] so that systematic bias in the results should be significant. The observed deviation between theory and experiment for 1 μm deep weirs was slightly larger than that for 3 μm deep weirs, but the precision of our data leads us to conclude that there is no measurable deviation from the predictions of the Navier–Stokes and Hagen–Poiseuille equations for flow in glass channels with a dimension ≥ 1 μm.

Table 1. Two-Port Channel Dimensions and Volume Conversion Factors

Device	W* (μm)	D_{in} (μm)	$L_{in} + L_{ex}$** (μm)	d_{wr} (μm)	L_{wr} (μm)	$k^{\dagger}$ (μm^2)
9A	294	10.25	35090	3.03	32.0	2.95×10^3
9D	293	10.20	34630	3.04	21.5	2.92×10^3
7A	290	10.05	35090	0.99	30.0	2.85×10^3
7D	290	9.96	34630	1.02	19.0	2.83×10^3

*The widths of the channel and the weir are the same.
**The total length of the inlet and exit segments.
†Conversion factor: observed linear velocity to volume flow rate.

Given that the Hagen–Poiseuille equation describes flow in these slot-shaped channels, it is simple to convert from the measured flow velocity to the volumetric flow rate, using $Q = k\overline{V}_z(0)$, where k is $FW^2/G(0)$, and $G(x)$, defined by inspection of Eq. 2, is evaluated at the center of the channel ($x = 0$). Specific values of k are given in Table 1.

Fluidic impedance of a flow channel network

We have combined two further tests of the Hagen–Poiseuille equation in the evaluation of a three-port device we used previously for the creation of chromatography and solid-phase extraction beds. Whereas our two-port devices contained slot-shaped channels, many fluidic devices use a D-shaped channel that results from isotropic etching of a mask feature that to a depth similar to the feature width. Our optical probe approach is not effective with such a channel because the y-direction velocity variation is significant relative to the laser probe spot size we used. However, measurement in a slot channel connected to a D-shaped channel should be effective, just as it is for measurement of flow across the very shallow weir. The tests described below show this is the case. Additionally, fluidic networks are a key component of most microfluidic chips, and passive control of flow distribution within a network is a key element of chip design. We have further tested the Hagen–Poiseuille equation by comparing the predicted flow distribution obtained for a three-port design, incorporating two weirs, a D-shaped channel, and a branched network with experimental measurements of the linear velocity distribution.

Figure 5 illustrates the three-port devices tested, and Table 3 provides the specific dimensions of each region of the device. The side channel was designed to have a sufficiently high resistance to flow compared to that of the weirs and the main channel to minimize flow into the side when pumping fluid along the main channel. We measured flow rates upstream and downstream of the two weirs, and compared them to determine the loss to the side channel. To compare the results with theory as accurately as possible we also needed to calculate the form factor F, for the isotropically etched side channel, and this was done using a computational fluid modeling package from Coventor.

The Hagen–Poiseuille equation may be expressed as $Q = \Delta p/r$, where r is the fluidic resistance of a flow channel seg-

Table 2. Comparison of Experimental Slopes with Those from the Navier–Stokes Equations for Two-Port Devices

Device	T (C)	η* (mPa · s)	R%**	Slope(cal)† (mm/kPa · s)	Slope(exp) (mm/kPa · s)	Dev%
9A	23.0	0.9416	3.4	0.256	0.254	0.8
9D	23.8	0.9205	2.3	0.266	0.271	−1.8
7A	23.0	0.9430	46.6	0.136	0.132	3.0
7D	23.0	0.9430	33.6	0.168	0.162	3.7

*The viscosity was calculated by $\eta = 1.793 \times 10^{-3} - 4.732 \times 10^{-5}T + 4.48 \times 10^{-7}T^2$, an empirical equation based on the data in Lide.[34]
**R% represents the contribution of the weir to the flow resistance.
†Slope(cal) was calculated by Eq. 9.

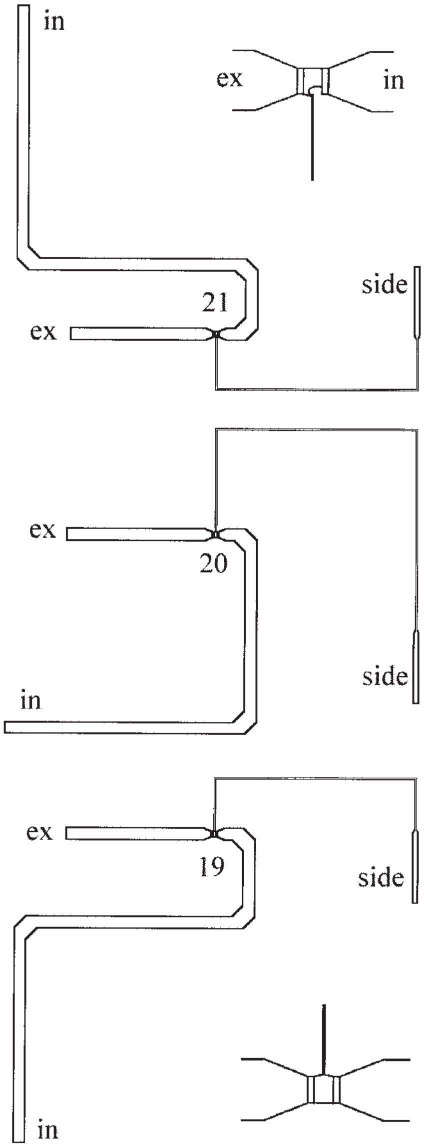

Figure 5. Layout of three-port devices tested.

Devices were numbered for identification, as shown. The pressure drops and dimension labels used in the analysis are shown. Most work was done using the symmetric side-channel connection to the double-weir zone (bottom inset), whereas some studies were performed using the asymmetric entrance to the double-weir zone (top inset).

ment, and $r = 4\eta L/(Wd)^2F$. We consider the point at the center of the main channel midway between the two weirs. The pressure drop between this point and either of the two exit ports is Δp, expressed for the main exit channel as

$$\Delta p = \Delta p_{ex} + \Delta p_{wr} \quad \text{or} \quad \Delta p = Q_{ex}r_{ex} + Q_{ex}r_{wr} \tag{12}$$

where subscript *ex* refers to the 10 μm deep exit channel (including the segment from the center of the channel to the weir) and *wr* to the weir region. The volume flow rate toward the exit port is the same in the 10 μm deep portion as it is across the weir. We can rearrange this expression to obtain

$$Q_{ex} = \Delta p/(r_{ex} + r_{wr}) \tag{13}$$

The side channel consists of a long, narrow segment (subscript 1) to restrict flow and a short, wide segment (subscript 2), allowing us to write

$$Q_s = \Delta p/(r_{s1} + r_{s2}) \tag{14}$$

The flow into the main channel exit, relative to the total flow from the main channel inlet, is given by

$$Q_{ex}/(Q_{ex} + Q_s) = Q_{ex}/Q_{in} = (r_{s1} + r_{s2})/(r_{ex} + r_{wr} + r_{s1} + r_{s2}) \tag{15}$$

where Q_{in} is the inlet channel flow. The value Q_{ex}/Q_{in} was evaluated experimentally by measuring the linear flow rate both upstream and downstream of the two weirs. Because the cross section of the main channel is the same at both measurement locations, the ratio of linear flow rates is equal to the ratio of volume flow rates, Q_{ex}/Q_{in}(exp). Figure 6 shows the linear flow velocities measured for weir depths of 1 and 3 μm. Table 4 presents the ratio of flow velocities for a series of devices, whose measured geometries are presented in Table 3. The data show that either decreasing the depth or increasing the length of the weir resulted in increased flow into the side arm, whereas

Table 3. Channel Dimensions (in μm) for Three-Port Devices

Device	*W*	*d*	*L*
819			
Exit channel	592	9.63	5997
Weir	273	3.16	21.5
Side channel 1	42.2	10.79	15,108
Side channel 2	225	10.79	2165
619			
Exit channel	590	9.61	5976
Weir	277	1.04	17.5
Side channel 1	43.8	10.74	15321
Side channel 2	235	10.74	2077
820			
Exit channel	592	9.71	5294
Weir	276	3.17	31.0
Side channel 1	41.2	10.81	25,282
Side channel 2	223	10.81	2059
720			
Exit channel	588	9.64	5343
Weir	274	1.00	32.0
Side channel 1	40.2	10.78	25,273
Side channel 2	222	10.78	1695
620			
Exit channel	593	9.65	5346
Weir	279	1.06	27.5
Side channel 1	43.8	10.84	25,312
Side channel 2	235	10.84	2194
921			
Exit channel	592	9.73	5351
Weir	275	3.03	30.0
Side channel 1	41.8	10.84	15,277
Side channel 2	223	10.84	2481
621			
Exit channel	593	9.68	5337
Weir	278	1.04	26.5
Side channel 1	44.0	10.76	15,287
Side channel 2	236	10.76	2055

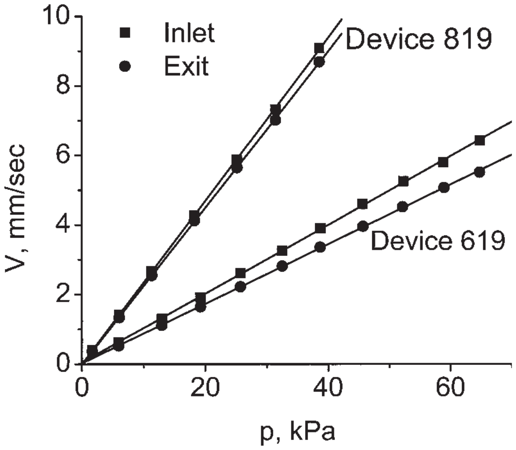

Figure 6. Plot of flow velocity vs. applied pressure.

Data are for $x19$ three-port devices, one with weirs etched 1.04 μm deep and 17.7 μm long (619) and the other with weirs etched 3.16 μm deep and 21.6 μm long (819). Top traces of each pair of curves (■) show the flow velocity upstream of the double weirs in the main channel, whereas bottom traces (●) show the velocity downstream of both weirs in the main channel. Bleaching laser 10–15 mW, detection laser 2.5 mW, PMT bias 500 V.

increasing the length of the side arm had the opposite effect (such as in device 620 vs. 621).

Form factor for D-shaped channels

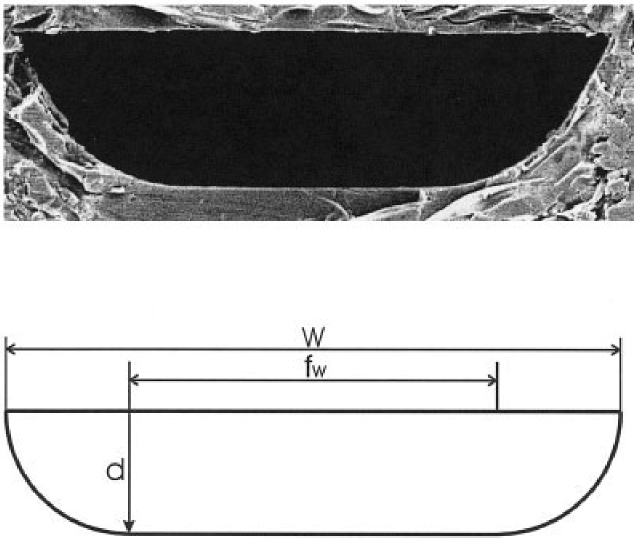

Figure 7. Electron micrograph of a typical D-shaped isotropically etched channel.

Dimension labels used for cross-sectional analysis are indicated.

To calculate r_{s1} and r_{s2} accurately the form factor F_D for an isotropically etched, D-shaped channel must be used, rather than the form factor for a rectangular channel given by Eq. 5. Because the D-shape is ubiquitous experimentally, we concluded that it would be useful to make available a working curve for its Hagen–Poiseuille equation form factor. Details regarding the stability and accuracy of the FEM simulation with Coventor's FlumeCAD are given in the Experimental section. Figure 7 shows an electron micrograph of a D-shaped channel, along with the notation used for the dimensions. The D-shape was taken to have width $W - 2d = fw$ at the bottom of the channel, W at the top, and a circular arc with radius d sweeping out the side walls, in good agreement with the photomicrograph. The aspect ratio, or d/W, is the critical variable in the form factor calculation, and we have compared channels having the same aspect ratio, as shown in Figure 8. The form factor F_D was calculated from $F_D = 4\eta LQ_{sim}/(Wd)^2\Delta p$, where Q_{sim} is the FEM simulated flow velocity. It is evident there are significant differences for d/W ratios $\gtrsim 0.05$. However, the differences are exaggerated by the different cross-sectional areas of the D-shape vs. rectangular shapes. We also show the form factor calculated according to $F_D = 4\eta LQ_{sim}/A^2\Delta p$, where A is the area of a D-shaped channel with aspect ratio d/W, demonstrating that if the area differences are normalized, the form factors differ only modestly. To facilitate the use of the working curve for a D-shaped channel, the results in Figure 8 for the bottom trace [$(Wd)^2$ normalization] were fit to the following empirical equation:

$$F_D = 0.3468\left(\frac{d}{W}\right) - 0.6230\left(\frac{d}{W}\right)^2 + 1.2466\left(\frac{d}{W}\right)^3 - 2.7916\left(\frac{d}{W}\right)^4 + 2.3696\left(\frac{d}{W}\right)^5 \quad (16)$$

Table 4. Comparison of the Experimental, Calculated, and Nominal Flow Ratios

Device	Q_{ex}/Q_{in}% (exp)	Q_{ex}/Q_{in}% (cal)*	Q_{ex}/Q_{in}% (nom)**	Q_{ex}/Q_{in}% (cal-exp)
819	96.0	96.8	98.3	+0.8
619	86.3	85.7	87.9	−0.6
820	98.5	98.2	99.0	−0.3
720	86.3	86.2	90.1	−0.1
620	86.9	87.7	90.3	+0.7
921	96.5	96.9	98.3	+0.4
621	81.6	80.8	84.9	−0.8

*Based on measured values of channel dimensions.
**Based on nominal values of channel dimensions.

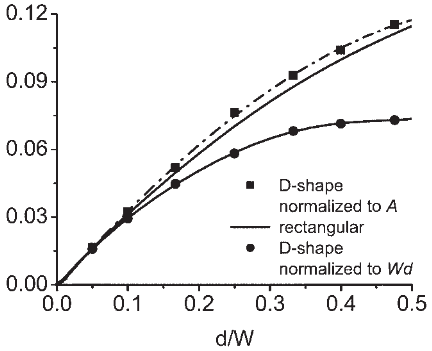

Figure 8. Plot of geometrical form factor (*F*) as a function of aspect ratio, depth/width (*d/W*).

Plot compares a rectangular cross section and for a D-shaped channel. F was calculated using Eq. 5 (—) for a rectangular channel shape. F for the D-shaped channel was calculated using $F_D = 4\eta LQ_{sim}/(Wd)^2\Delta p$ for the bottom trace (●) and $F_D = 4\eta LQ_{sim}/A^2\Delta p$ (A is area) for the topmost trace (■). The bottom curve was fit with Eq. 16 to provide a working curve for F_D.

Equation 16 gives an RSD of $<0.5\%$ ($r^2 = 0.9998$) for aspect ratios between 0.05 to 0.5, compared to the numerically calculated data points in Figure 8.

Applicability of the Hagen–Poiseuille equation in modeling a fluidic network

The fluid flow within the three-port device could be evaluated using the Hagen–Poiseuille equation, along with the form factors given by Eq. 16 for a D-shaped channel and Eq. 5 for the slot-shaped channels. Again, taking the pressure drop from the center of the main channel midway between the two weirs to atmosphere as Δp, we use Eqs. 13–15 to calculate the ratio predicted for Q_{ex}/Q_{in}(cal). The resulting values are given in Table 4, along with the deviation relative to the experimentally observed ratio, Q_{ex}/Q_{in}(exp). The deviation in Table 4 is smaller than that seen in Table 2, presumably because the error of a relative flow rate is less susceptible to measurement bias than is the absolute flow rate. The comparison shows that the Hagen–Poiseuille equation accurately predicts the ratio of flows at the branching point in the channel, even with a 1 μm sized flow channel as one of the design components.

The value for Q_{ex}/Q_{in}(cal) was determined using measured values of the device dimensions, rather than the nominal values targeted by the fabrication process. Because variations in etch depths and channel lengths do occur from batch to batch, and even within a single wafer, it is instructive to evaluate how great an effect this can have on the deviation between experiment and theory. The value for Q_{ex}/Q_{in}(nominal) was calculated assuming etch depths of 10 μm for the deep channel, 1 or 3 μm for the weirs, and a 1:1 aspect ratio for isotropic etching, using the feature widths of the mask design. The side channel form factor was evaluated for a D-shape, and the other channels were taken to be rectangular. A comparison in Table 4 of Q_{ex}/Q_{in}(nominal) with Q_{ex}/Q_{in}(cal) predicted for actual dimensions shows a deviation of 1–4%, as does a comparison to the measured flow rates, Q_{ex}/Q_{in}(exp). This result provides a useful estimation of the tolerance that can be expected in performance from fabricated flow restrictors, relative to the design parameters.

Conclusions

The photobleaching, time-of-flight procedure used here provides measurement of the linear velocity of flow rates in microchip devices with small dimensions and offers a useful alternative to PIV techniques, which are not well suited to low-micrometer– and submicrometer-scale devices. Solutions to the Navier–Stokes equations were developed that successfully converted volumetric flow rates to linear velocities, so that the measured values could be compared quantitatively to the predictions of the Hagen–Poiseuille equation. The Navier–Stokes equation and the Hagen–Poiseuille solution to it successfully describe the pressure–flow rate relationship in devices with at least one dimension on the scale of 1 μm. This contrasts with claims of a variety of previous studies,[6-12] but is consistent with most researchers' expectations.[4,5,13,14] The model was tested across a linear flow rate range in the narrowest dimension of 0.3 to 16 mm/s and a volumetric flow rate range of 0.6 to 32 nL/s. The maximum Reynolds number tested was 0.3. The Hagen–Poiseuille solution can be used to design multiport devices with intersecting channels, achieving the intended flow rate ratios in channels with differing flow resistance with an accuracy of 1–2%. Despite the differences between achieved etched dimensions and the nominal design values a deviation of only 1–4% in the flow ratios was also achieved. This observation provides a useful guideline for predicting tolerance sensitivity in device manufacture. Finally, the empirical equation for the geometric form factor of a D-shaped channel should provide a useful working curve for use of the Hagen–Poiseuille equation in microfluidics design.

Acknowledgements

We thank the Natural Sciences and Engineering Research Council of Canada for funding, the University of Alberta for support of the NanoFab lab, and Coventor for kind donation of FlumeCAD software. We thank the Chemistry Department Shops for custom-built instrumentation.

Literature Cited

1. Harrison DJ, Fluri K, Seiler K, Fan Z, Effenhauser CS, Manz A. Micromachining a miniaturized capillary electrophoresis-based chemical analysis system on a chip. *Science* 1993;261:895-898.
2. Longwell PA. *Mechanics of Fluid Flow.* New York, NY: McGraw-Hill; 1966.
3. Johnson RW. *The Handbook of Fluid Dynamics.* Boca Raton, FL: CRC Press; 1998.
4. Stone HA, Stroock AD, Ajdari A. Engineering flows in small devices: Microfluidics toward a lab-on-a-chip. *Annu Rev Fluid Mech.* 2004;36: 381-411.
5. Squires TM, Quake SR. Microfluidics: Fluid physics at the nanoliter scale. *Rev Mod Phys* 2005;77: in press.
6. Pfahler J, Harley J, Bau H, Zemel J. Liquid transport in micron and submicron channels. *Sens Actuators A.* 1990;21–23:431-434.
7. Peng XF, Peterson GP, Wang BX. Frictional flow characteristics of water flowing through rectangular microchannels. *Exp Heat Transfer.* 1994;7:249-264.
8. Mala GM, Li D. Flow characteristics of water in microtubes. *Int J Heat Fluid Flow.* 1999;20:142-148.
9. Papautsky I, Brazzle J, Ameel T, Frazier AB. Laminar fluid behavior in microchannels using micropolar fluid theory. *Sens Actuators A.* 1999;73:101-108.
10. Sharp KV, Adrian RJ, Beebe DJ. Anomalous transition to turbulence in microtubes. Proc of 2000 ASME International Mechanical Engineering Congress & Exposition, Orlando, FL, MEMS Vol. 2. 2000: 461-466.
11. Ren L, Qu W, Li D. Interfacial electrokinetic effects on liquid flow in microchannels. *Int J Heat Mass Transfer.* 2001;44:3125-3134.
12. Brutin D, Topin F, Tadrist L. Transient method for the liquid laminar flow friction factor in microtubes. *AIChE J.* 2003;49:2759-2767.
13. Kohl MJ, Abdel-Khalik SI, Jeter SM, Sadowski DL. An experimental investigation of microchannel flow with internal pressure measurements. *Int J Heat Mass Transfer.* 2005;48:1518-1533.
14. Choi CH, Westin KJA, Breuer KS. Apparent slip flows in hydrophilic and hydrophobic microchannels. *Phys Fluids.* 2003;15:2897-2902.
15. Chen Z, Milner TE, Dave D, Nelson JS. Optical Doppler tomographic imaging of fluid flow velocity in highly scattering media. *Opt Lett.* 1997;22:64-66.
16. Santiago JG, Wereley S, Meinhart CD, Beebe DJ, Adrain RJ. A micro particle image velocimetry system. *Exp Fluids.* 1998;25:316-319.
17. Drain LE. *The Laser Doppler Technique.* Chichester, UK: Wiley; 1980.
18. Wang W, Lui Y, Sonek GJ, Berns MW, Keller RA. Optical trapping and fluorescence detection in laminar flow streams. *Appl Phys Lett.* 1995;67:1057-1059.
19. Monnig CA, Jorgenson JW. On-column sample gating for high-speed capillary zone electrophoresis. *Anal Chem.* 1991;63:802-807.
20. Monnig CA, Dohmeier DM, Jorgenson JW. Sample gating in open tubular and packed capillaries for high-speed liquid chromatography. *Anal Chem.* 1991;63:807-810.
21. Moore AW Jr, Jorgenson JW. Study of zone broadening in optically gated high-speed capillary electrophoresis. *Anal Chem.* 1993;65:3550-3560.

22. Oleschuk RD, Shultz-Lockyear LL, Ning Y, Harrison DJ. Trapping of bead-based reagents within microfluidic systems: On-chip solid-phase extraction and electrochromatography. *Anal Chem.* 2000;72:585-590.
23. Oleschuk RD, Jemere AB, Shultz-Lockyear LL, Fajuyigbe F, Harrison DJ. Utilization of bead based reagents in microfluidic systems. *Proceedings of Micro Total Analysis Systems 2000.* Dordrecht, The Netherlands: Kluwer Academic; 2000:11-14.
24. Fan ZH, Harrison DJ. Micromachining of capillary electrophoresis injectors and separators on glass chips and evaluation of flow at capillary intersections. *Anal Chem.* 1994;66:177-184.
25. Baker AJ. *Finite Element Computational Fluid Mechanics.* Washington, DC: Hemisphere; 1983.
26. Neckers DC, Valdes-Aguilera OM. Photochemistry of the xanthene dyes. *Adv Photochem.* 1993;18:315-394.
27. Lindquist L. A flash photolysis study of fluorescein. *Arkiv Kemi.* 1960;16:79-138.
28. Kasche V, Lindquist L. Reactions between the triplet state of fluorescein and oxygen. *J Phys Chem.* 1964;68:817-823.
29. Ocvirk G, Tang T, Harrison DJ. Optimization of confocal epifluorescence microscopy for microchip-based miniaturized total analysis systems. *Analyst.* 1998;123:1429-1434.
30. *FlumeCAD Guide.* Raleigh, NC: Coventor Technologies, Inc.; 2000.
31. Friedmann M, Gillis J, Liron N. Laminar flow in a pipe at low and moderate Reynolds numbers. *Appl Sci Res.* 1968;19:426-438.
32. Ward-Smith AJ. *Internal Fluid Flow: The Fluid Dynamics of Flow Pipes and Ducts.* Oxford, UK: Clarendon; 1980.
33. Probstein RF. *Physicochemical Hydrodynamics: An Introduction*. 2nd Edition. New York, NY: Wiley; 1994.
34. Lide DR, ed. *Handbook of Chemistry and Physics.* 83rd Edition. Boca Raton, FL: CRC Press; 2002–2003.
35. Wu S, Dovichi NJ. Fresnal diffraction theory for steady-state thermal lens measurements in thin films. *J Appl Phys.* 1990;67:1170-1182.

Manuscript received Mar. 4, 2005, and revision received May 26, 2005.